

Preferential Pt Nanocluster Seeding at Grain Boundaries Dislocations in Polycrystalline Monolayer MoS₂

Shanshan Wang^{1,2}, Hidetaka Sawada³, Si Zhou¹, Sha Li¹, Angus I. Kirkland^{1,4}, Jamie H. Warner¹

¹Department of Materials, 16 Parks Road, University of Oxford, OX1 3PH, UK

²State Key Laboratory of Advanced Ceramic Fibers & Composites, College of Aerospace, National University of Defense Technology, Changsha 410073, Hunan Province, P.R. China

³JEOL Ltd., 3-1-2 Musashino, Akishima, Tokyo 196-8558, Japan

⁴Electron Physical Sciences Imaging Center, Diamond Light Source Ltd, Didcot, UK

Abstract

We show that Pt nanoclusters preferentially nucleate along the grain boundaries (GBs) in polycrystalline MoS₂ monolayer films, with dislocations acting as the seed site. Atomic resolution studies by aberration-corrected annular dark field scanning transmission electron microscopy reveal periodic spacing of Pt nanoclusters with dependence on GB tilt angles and random spacings for the anti-phase boundaries (i.e. 60°). Individual Pt atoms are imaged within the dislocation core sections of the GB region, with various positions observed, including both the substitutional sites of Mo and the hollow center of the octahedral ring. The evolution from single atoms, small few atom clusters to nanosized particles of Pt is examined at the atomic level to gain a deep understanding of the pathways of Pt seed nucleation and growth at the GB. DFT calculations confirm the energetic advantage of trapping Pt at dislocations on both the APB and the small-angle GB rather than on the pristine lattice.

The selective decoration of GBs by Pt nanoparticles also has a beneficial use to easily identify GB

areas during microscopic scale observations and track long range nanoscale variances of GBs with spatial detail not easy to achieve using other methods. We show that GBs have nanoscale meandering across micron scale distances with no strong preference for specific lattice directions across macroscopic ranges.

KEYWORDS: Pt dopants, Grain boundary, MoS₂, ADF-STEM, 2D materials

Monolayer molybdenum disulfide (MoS₂) is a two-dimensional (2D) semiconducting material, composed of one layer of Mo atoms sandwiched between two layers of S atoms through covalent bonds, and holds great potential in applications of nanoelectronics, optoelectronics and catalysis.¹⁻⁸ Chemical vapor deposition (CVD) has emerged as one of the most promising approaches to satisfy the industrial requirements on both high quality and productivity of this material. Although wafer-scale, continuous monolayer MoS₂ have already been synthesized, they are commonly polycrystalline sheets with grain size in the order of several micrometers, in which grain boundaries (GBs) are inevitably and can influence the overall properties of the material profoundly.⁹⁻¹⁴ Band structures can be largely tuned with implantations of mid-gap states depending on the atomic stitching manner between grains by theoretical calculations, while electrical transport and photoluminescence emission characteristics (PL peak energy, intensity and width) of monolayer MoS₂ have been confirmed to be altered by GBs through experimental studies.^{15,16} Therefore, characterizing and understanding GBs is significant for the manipulation of properties of 2D materials, including MoS₂.

Several methods have been established to probe GBs of 2D materials. In the macroscopic scale, a liquid crystalline texture method was applied to directly visualize MoS₂ and graphene GBs under the polarized optical microscope based on the correspondence between the orientation of liquid crystals

and that of the underlying 2D material.^{17,18} The selective oxidation of the underlying copper substrate through functionalized graphene GBs grown on top was used to probe graphene GBs just using the optical microscope.¹⁹ Photoluminescence, Raman and multiphoton microscopy were also utilized to discriminate GBs of MoS₂ macroscopically by constructing 2D maps and detecting subtle variations of the peak position and intensity at GBs.^{16,20} These methods can display the concentration and distribution of GBs in a large area. However, they are mainly limited in supplying detailed information about the atomic structures of GBs and the misorientation angle between neighboring grains. Some methods also suffer from the low sensitivity when the GB angle is small. Annular dark field scanning transmission electron microscopy (ADF-STEM) can resolve GB configurations down to the atomic level. Several structures have been discovered, typically including arrays of 5- and 7-fold (5|7) rings, 6|8 rings and 4|6 rings with slight variations on element types at different lattice points for small-angle GBs, as well as linearly arranged 4-fold rings with point sharing (4|4P) or edge sharing (4|4E) and the recurring 8|4|4 motif for anti-phase boundaries (APBs), i.e 60° rotation.^{15,16,21} However, due to the nanoscale width of GBs, the relatively low concentration of them compared with the pristine lattice and the small characterization region of high-resolution ADF-STEM, directly locating GBs on monolayer MoS₂ at the microscopic level using ADF-STEM is time-consuming and challenging. Therefore, developing methods that can visualize both the atomic configurations of GBs microscopically and their geometry and distribution macroscopically with fast speed, convenient operation and high sensitivity is highly desirable.

Apart from the investigation of GBs, comprehension about the interaction between single foreign atoms and the host 2D crystal is also critical for tailoring materials' electrical and catalytic properties.

ADF-STEM has contrast that is sensitive to the atomic number of the column being probed and enables both the detailed bonding configuration and the element of dopants on the host 2D crystal to be unambiguously identified.^{22–27} Both Re and Au dopants have been successfully introduced to single layer MoS₂, which substituted or resided on various atomic sites, including Mo, S and hollow centers of hexagonal rings, and led to n-type and p-type doping, respectively.²⁸ Recent work has studied the atomic structure of single Pt atoms on the surface of MoS₂ and found that Pt prefers to localize in S vacancy sites on monolayer MoS₂ due to increased binding energy. This was then calculated by density functional theory to show a detrimental impact on the surface catalytic activity for hydrogen evolution reaction (HER).²⁹ In addition, Cr and V impurity dopants have been found in CVD-grown monolayer MoS₂ and behave as substitutional atoms at the Mo sites, resulting in n-type doping commonly seen in CVD-grown transition metal dichalcogenide (TMD) samples.³⁰ However, most studies have focused on single atom dopants on pristine monolayer MoS₂, with little work done on dopants interacting with defective structures, such as GBs. Prior work has shown that Pt can preferentially form nanoclusters in grain boundary regions of graphene using electron diffraction in an electron microscope, but the detailed atomic level imaging of Pt atoms interacting with dislocation cores was not experimentally performed, but was theoretically predicted.³¹

Here, we show how Pt nanoclusters preferentially nucleate at dislocation cores in GB regions of MoS₂. This leads to a simple strategy to quickly locate GBs in CVD-grown polycrystalline monolayer MoS₂ by the selective decoration of Pt nanocrystals on GBs. This is achieved by depositing a Pt precursor followed by decomposing it at high temperature to form Pt nanocrystals. Different Pt nanoparticle formation is examined at small-angle GBs and APBs, respectively. The inter-particle

distance is quantitatively dependent upon the misorientation angle between adjacent grains, matching predictions based on the Frank-Bilby equation.^{32–36} Moreover, these dislocation cores at small-angle GBs perform as a template to construct a 1D Pt nanoparticle chain with an even spacing, which has a potential for applications of waveguiding, surface-enhanced Raman scattering and gas sensing.^{37–39}

Results and Discussion

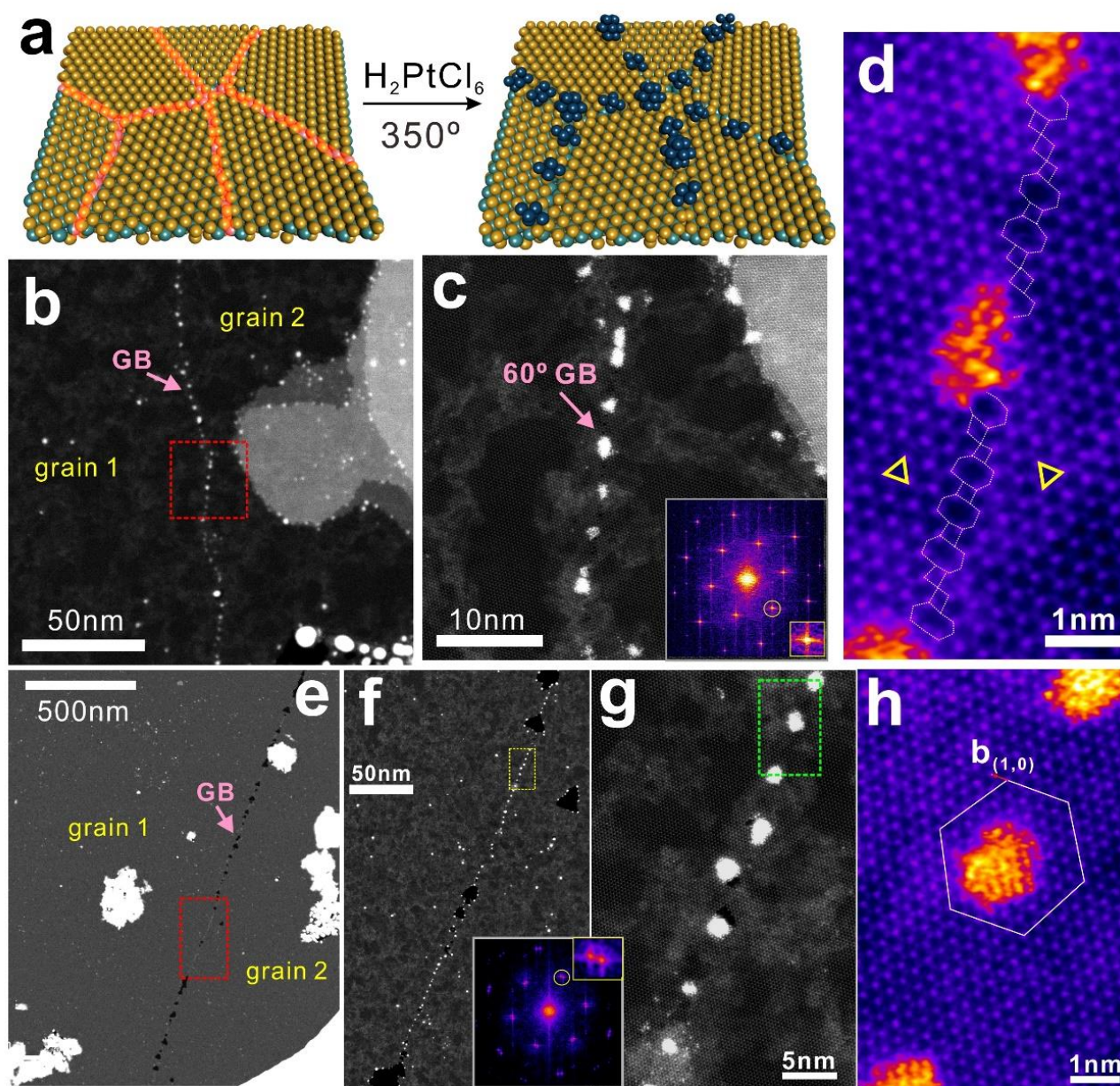


Figure 1. (a) Schematic illustration of decorating GBs of monolayer MoS₂ with Pt nanocrystals. (b) Low-mag ADF-STEM image showing the deposition of Pt nanocrystals on a APB. (c) Zoomed-in ADF-STEM image of

the region marked with the red box in (b). Inset is the FFT of (c), in which only one set of reflexes can be observed. (d) High-mag ADF-STEM image showing the detailed atomic structure of the Pt-decorated APB corresponding to (c), where Pt nanocrystals discretely attach on a periodic line 8-fold and 4-fold rings, as outlined with white lines. (e) Low-mag ADF-STEM image of a small-angle GB composed of Pt nanocrystal deposition and triangular-shaped nanopores. (f) Zoomed-in ADF-STEM image of the area labelled by the red box in (e). Inset is the FFT of (e), in which two sets of MoS₂ reflexes are displayed with a misorientation angle of $\sim 3.6^\circ$. (g) Medium-mag ADF-STEM image corresponding to the yellow boxed region in (f), indicating a uniform distribution of Pt nanocrystals along the small-angle GB. (h) High-mag ADF-STEM image of the green-boxed region in (g), showing that the Pt nanocrystal is deposited on a dislocation core on the small-angle GB with a Burgers vector **b** and closed circuit (white) surrounding it.

Monolayer MoS₂ was grown by CVD followed by being transferred onto a Si₃N₄ TEM grid using a polymer-assisted method previously reported.^{40–42} Subsequently, a drop of diluted H₂PtCl₆/ethanol solution (0.025mol/L) was deposited on the grid and allowed to dry in the air naturally. Finally, the grid was heated at 350° C under the protection of Ar gas at atmospheric pressure for 15 min to decompose the Pt precursor so that Pt particles with diameters of several nanometers can be obtained on the surface of monolayer MoS₂. We found that Pt nanoparticles are prone to anchoring and aligning on GBs of MoS₂, as schematically illustrated in Figure 1a. The Pt nanocrystals attached on GBs adopt much higher brightness compared with the pristine monolayer MoS₂ lattice, serving as indicators to tell the exact location of GBs even under a low-magnification imaging condition and exhibiting the morphology of GBs in a large scale. Figure 1b-d show the configuration of a Pt-decorated APB, where two neighboring grains are twisted by an integral multiple of 60°, with an increased magnification of ADF-STEM images. The relative lattice orientation between two grains can be indicated by the fast Fourier transform (FFT) of the ADF-STEM image, where only one set of reflexes were observed (inset

of Figure 1c). It can also be fully confirmed by the detailed structure of the 6-fold rings on two sides of the GB in the high-mag image, in which positions of Mo and S atoms are swapped in the hexagonal lattice (yellow triangles in Figure 1d). The APB winds its way across the monolayer MoS₂ region in the nanometer scale (Figure 1b) with Pt nanoparticles unevenly deposited on it (Figure 1c). With the help of the high-mag ADF-STEM image in Figure 1d, it shows that the APB is composed of an array of randomly combined octagonal and tetragonal rings, and Pt nanocrystals are arbitrarily deposited on the linearly extended APB. Figure 1e-h shows another scenario, where Pt nanocrystals decorate on a small-angle GB with grain orientation mismatch of $\sim 3.6^\circ$, as evidenced by the FFT of Figure 1f. The GB appears straight in the micrometer scale but can be sinuous in the nanometer scale (Figure S1). It is decorated by not only arrays of Pt nanoparticles but also chains of triangular holes with a broad size distribution (Figure S2, Figure S4). The generation of well-shaped holes might be ascribed to the superiority in the chemical reactivity of dislocation cores on small-angle GBs over the intrinsic MoS₂ lattice, so that atoms are more easily to be etched by components in the air, such as O₂ and H₂O, or during the heat treatment for the decomposition of the Pt precursor along energetically favorable lattice orientations.⁴³ The frequency of holes in the APB is significantly lower than that on small-angle GBs. Distinct from the case of APB, a majority of Pt nanoparticles are uniformly spaced on the small-angle GB (Figure 1g), and their inter-particle distance is associated with the GB misorientation angle, which will be discussed in detail in Figure 2. By constructing the Burgers circuit that encloses a Pt nanocrystal, we can get the Burgers vector to be (1,0), which is the shortest one for a perfect edge dislocation formed by the insertion or removal of a semi-infinite row of atoms along the armchair direction (Figure 1h). It proves that these Pt nanocrystals are selectively anchored on the dislocation cores of the small-

angle GB rather than on pristine MoS₂ lattice, which could be attributed to the change of the coordination manner of Mo and S atoms at dislocation cores so that the binding energy between Pt and the MoS₂ at the defective region can be increased. This could also explain the reason why the concentration of Pt nanoparticles on GBs, no matter whether they are APBs or small-angle GBs, surpasses that within grains predominantly. Even the existence of edges, which is well known as highly active nucleation sites, did not influence the selective deposition of Pt nanocrystals on GBs (Figure 1b).

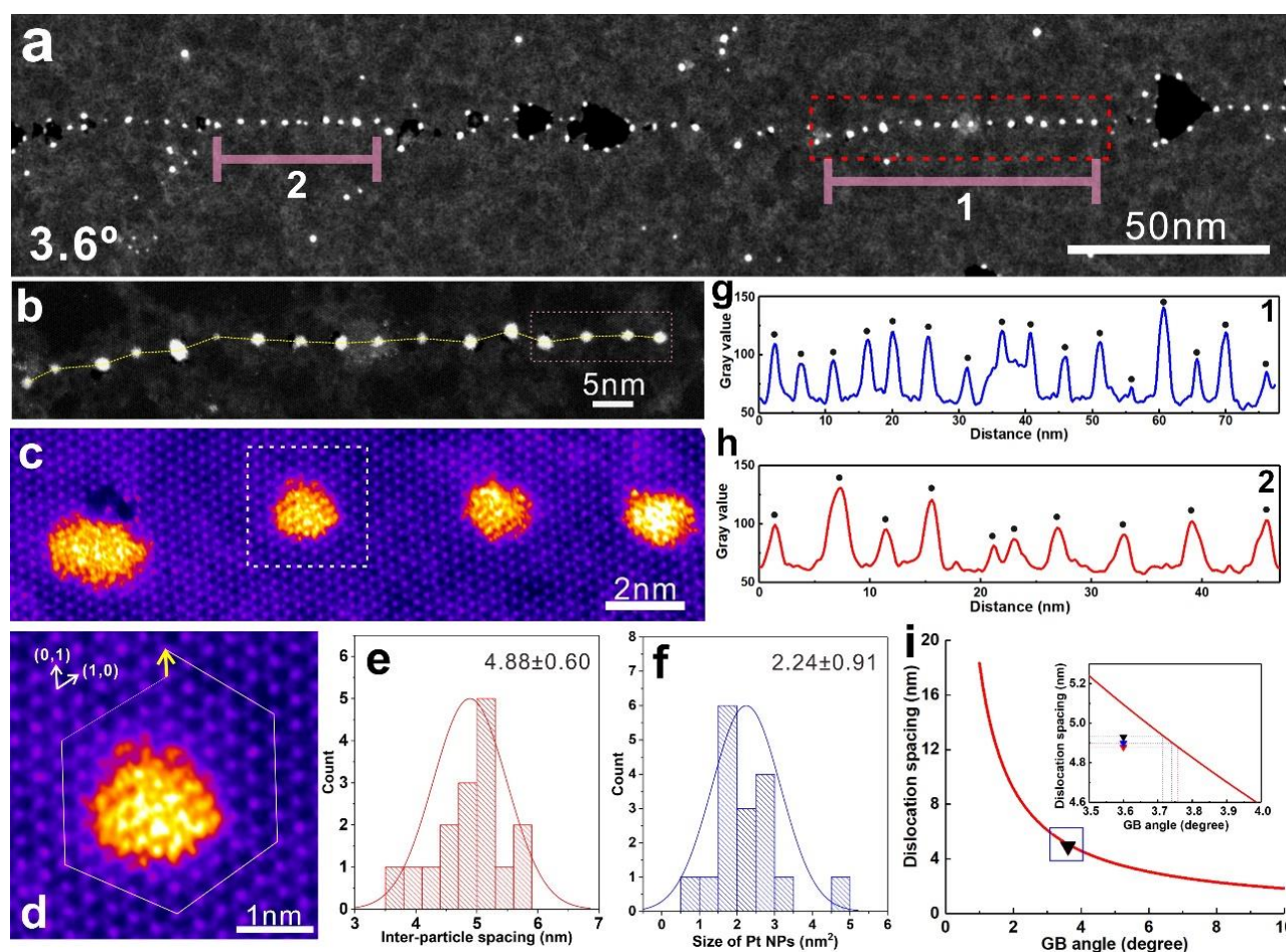


Figure 2. (a) Zoomed-in ADF-STEM image showing the Pt-decorated small-angle GB corresponding to Figure 1(f). (b) Magnified image of the region marked with the red box in (a). (c) Medium-mag ADF-STEM image corresponding to the pink box in (b). (d) High-mag ADF-STEM image of the white-boxed region in (c) with the Burgers vector (yellow arrow) and the closed circuit (white) labelled. (e) Distribution of inter-particle spacing of Pt nanocrystals attached on the small-

angle GB based on the measurement of the distance between adjacent Pt nanoparticles in (b), as indicated by the yellow dashed lines. (f) Distribution of the Pt nanocrystal size deposited on the small-angle GB in (b). (g,h) Intensity line profiles measured along two pink segments across the linearly-distributed Pt nanocrystal chains on the GB in (a), marked by 1 and 2, respectively. Location of each Pt nanoparticle can be clearly detected due to the prominent contrast variations so that the average distance between neighboring nanocrystals can be calculated. (i) Plot showing the dislocation spacing as a function of the misorientation angle between adjacent grains based on the Frank-Bilby equation, which is applied to small-angle GBs. Inset is the zoomed-in image of the blue boxed region. Red, black and blue data points with coordinates of (4.88, 3.6), (4.93, 3.6) and (4.90, 3.6) calculated from the experimental data in (e), (g) and (h), respectively, agrees with the Frank-Bilby curve well.

Figure 2a is the magnified ADF-STEM image showing the Pt-decorated small-angle GB in Figure 1f. Figure 2b corresponds to the region in the red dashed box in Figure 2a, where a chain of Pt nanocrystals arranged with an almost uniform spacing are aligned on the GB with a misorientation angle of $\sim 3.6^\circ$. Figure 2c is the magnified image of the pink-boxed region in Figure 2b with a false color look-up table (LUT) to enhance the visualization of Pt nanoparticles with respect to the MoS₂ lattice. Most Pt nanocrystals are residing on the intact MoS₂ film without pores surrounding them. Only a small number of Pt nanocrystals sit within nanopores, which could be formed either by the Pt-catalyzed chemical etching of MoS₂ during the heat treatment or by the dislocation core-induced decomposition of the MoS₂ film to release strain. The Burgers vector and the closed circuits around another Pt nanocrystal corresponding to the white-boxed region in Figure 2c, are shown in Figure 2d. It displays the same length of the Burgers vector, indicating a similar type of edge dislocation where Pt nanoparticles selectively anchor. The mean inter-particle spacing of Pt nanocrystals measured by the yellow dashed lines in Figure 2b is 4.88 nm with a standard error of ± 0.60 nm (Figure 2e), while the geometric mean size of the Pt nanoparticles is 2.24 nm² with a standard error of 0.91 nm² (Figure

2f) for this small-angle GB with a GB angle of 3.6° . The variation of the Pt nanoparticle size could be induced by several factors, including the thermal decomposition condition for Pt-precursor, the dislocation structure in GBs, the distribution uniformity of Pt-precursor, and the hydrocarbon contamination on the MoS₂ surface, etc. It is well-documented that the atomically-stitched small-angle GB in MoS₂ is constructed by an array of discrete dislocation cores.^{15,16} In bulk materials, the relationship between the spacing of dislocation cores in small-angle GBs ($<10^\circ$) and the misorientation angle of adjacent grains is commonly expressed by the well-known Frank-Bilby equation,³²⁻³⁶ given as $d=b/[2\sin(\theta/2)]$ in a 2D regime, in which d represents the average dislocation spacing, b is the magnitude of the Burgers vector for the edge dislocations on the GB and θ is the GB angle. For dislocation cores in small-angle GBs of monolayer MoS₂, b is a constant with a magnitude of 0.312 nm, as evidenced by the former analysis in Figure 1h and 2d and other literatures.^{16,35,43} It has been shown that Pt nanocrystals prefer to attach on the discrete dislocation cores. Therefore, the average spacing between dislocations can be equivalently obtained by the measurement of the inter-particle distance between Pt nanoparticles. We show a plot of the dislocation spacing (d) as a function of the GB angle (θ) according to the Frank-Bilby equation in Figure 2i, with its inset providing the magnified view corresponding to the blue-boxed region. It shows that the data point (red spot) with coordinates of (4.88, 3.6) based on the measurement in Figure 2e is well consistent with the Frank-Bilby curve. This indicates that a quantitative relationship of the GB angle and the inter-particle spacing between Pt nanocrystals on the GB can be established. It can transform the measurement of the small GB angle, which sometimes is not easy to detect without the diffraction information (such as using SEM and low-mag (S)TEM imaging), to the characterization of the average distance between neighboring Pt

nanocrystals selectively decorated on the small-angle GB. To verify the feasibility of estimating the small GB angle by measuring the average interparticle distance in a low-mag image, we drew intensity line profiles along two pink segments across the linearly-distributed Pt nanoparticle chains on the small-angle GB in a low-mag ADF-STEM image (Figure 2a), as labelled by 1 and 2, respectively (section S9 in SI). Location of each Pt nanoparticle can be clearly detected due to the prominent contrast variations so that the average distance between neighboring nanocrystals can be calculated, yielding 4.93 nm and 4.90 nm, respectively. The GB angles calculated from these two values of the average Pt nanocrystal spacing, based on the Frank-Bilby equation, are 3.71° and 3.74° (blue and black spots in Figure 2i), both of which are very close to the GB angle directly measured from the FFT of the high-mag ADF-STEM image, which is 3.6° . Therefore, the feasibility of evaluating the small misorientation angle between grains by using the Pt nanoclusters on the MoS₂ sample and measuring the inter-particle spacing between Pt nanoclusters selectively decorated on GBs is verified.

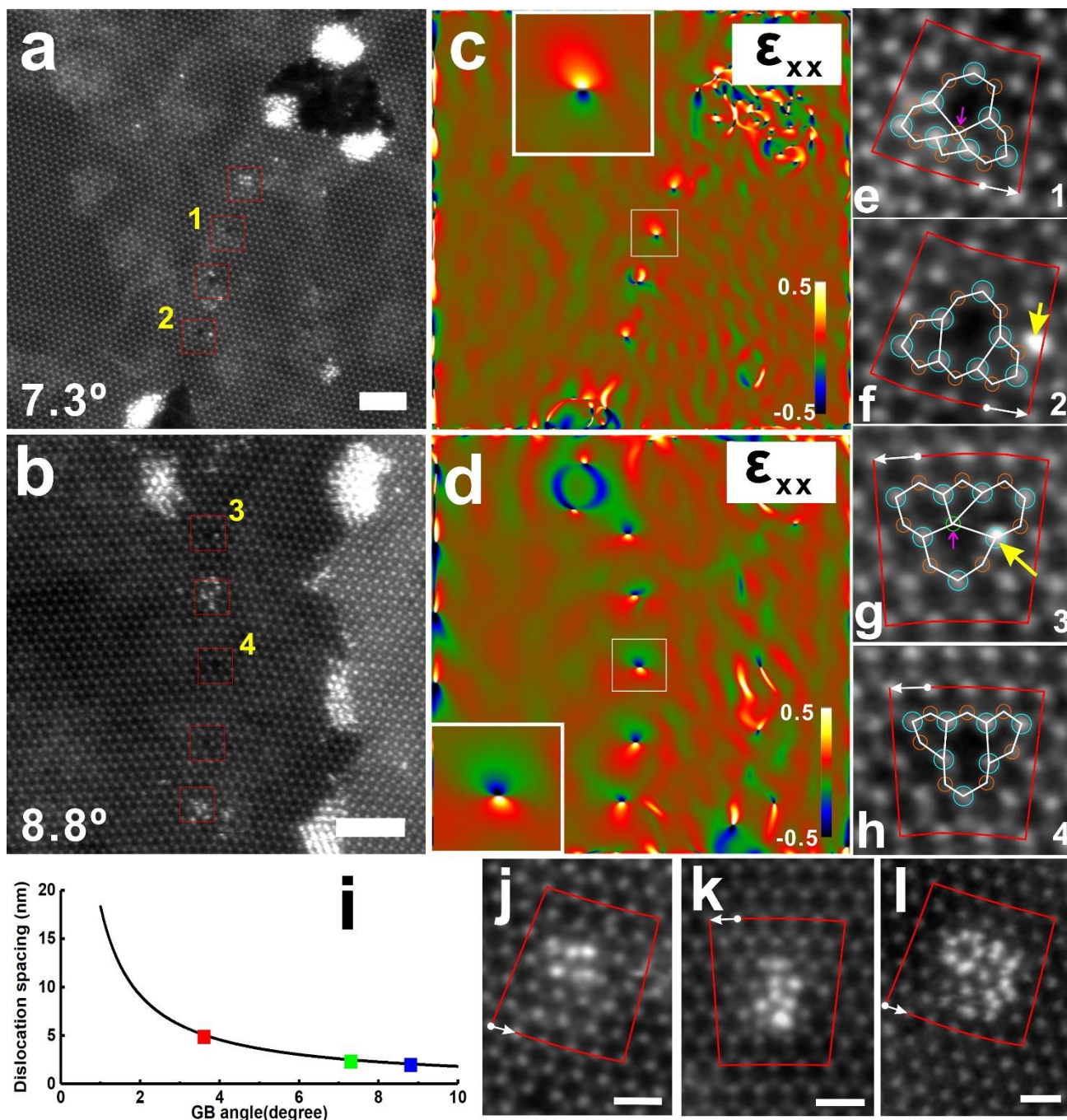


Figure 3. (a,b) ADF-STEM images showing two small-angle GBs with misorientation angles of $\sim 7.3^\circ$ and $\sim 8.8^\circ$, respectively. Scale bars: 2nm. (c,d) 2D strain maps of ϵ_{xx} corresponding to (a) and (b), respectively, with a color scale ranging from -0.5 to +0.5. Insets are the zoomed-in strain maps of the white-boxed regions in (c) and (d), respectively, highlighting the tension-compression dipoles existing at dislocation cores on GBs. (e-h) Higher magnification ADF-STEM images showing the atomic configurations of dislocation cores in red boxes marked from 1 to 4 in (a) and (b), respectively, with atomic models overlaid, as well as Burgers vectors (white arrows) and closed circuits (red) labelled. Mo and S atoms are represented by cyan and orange circles, respectively. Surrounding Pt dopants are pointed out by yellow arrows. (i) Plot

of dislocation spacing as a function of the GB angle with three experimental data points measured based on figure 2e (red), figure 3(c) (green) and figure 3(d) (blue), respectively. The dislocation spacing in (c) and (d) are obtained by measuring the distances between the centers of neighboring tension-compression dipoles and averaging them. (j-k) Higher magnification ADF-STEM images showing ultra-small Pt clusters aggregating on the dislocation core of small angle GBs. Scale bars: 0.5nm.

To investigate the atomic structure of dislocation cores on the small-angle GB, which attract the deposition of Pt nanocrystals, we found some dislocation cores aligned on the GB with various misorientation angles, which are not covered by Pt clusters, as marked by red boxes in Figure 3a and 3b. They may not be conspicuous in the medium-mag ADF-STEM images. However, with the help of geometric phase analysis (GPA), we can map the 2D strain field distribution of the whole image, in which dislocation cores on the GB exhibit peculiar characteristics (Figure S3). As shown in Figure 3c and 3d, the ϵ_{xx} strain field surrounding each dislocation core exhibits a two-lobed configuration, composed of a tension-compression dipole with similar magnitudes and the extent of the spatial dispersion. The strain fields are localized around each dislocation core on the small-angle GB without penetrating into the neighboring grains deeply. In addition, the strain fields of adjacent dislocation cores do not intersect with each other under the present case of dislocation spacing, which might contribute to the spatial stabilization of these isolated dislocations. The average distance between neighboring dislocations corresponding to the GB angle of 7.3° and 8.8° , respectively, can be conveniently measured from the 2D strain maps of Figure 3c and 3d, yielding 2.31 nm and 1.97 nm, respectively, marked as green and blue data points in Figure 3i. Both these two points together with the red point measured from Figure 2e agree with the Frank-Bilby equation well under different cases of small GB angles, indicating a wider range of application of evaluating the small GB angle by

measuring the spacing of dislocation cores decorated by Pt nanoparticles.

To resolve the atomic structure of dislocation cores, regions marked from 1 to 4 are magnified with atomic models overlapped with cyan and orange circles representing Mo and S atoms, respectively, as shown in Figure 3e to 3h. The dislocation cores primarily consist of 4- and 6-membered rings joined at S sites with an unusual 4-fold coordination manner distinct from the case in the pristine MoS₂ lattice, as pointed by the magenta arrows in Figure 3e and 3g. Two 6-fold rings at shoulders of the 4|6 dislocation core are seriously distorted. If the S atom at the intersection is missing, the dislocation reconstructs to the 5|8|5 structure, composed of double 5-fold rings stitching at two sides of the 8-fold ring with Mo-Mo edge sharing, as illustrated in Figure 3f and 3h. Burgers circuits and vectors for each dislocation were drawn by red curves and white arrows, suggesting that edge components of Burgers vectors corresponding to all four dislocation cores with various configurations are the same, being 0.312nm. This supports the validity of treating the Burgers vector b as a constant when plotting the dislocation spacing as a function of the GB angle in Figure 2i and 3i. Single Pt atom dopants were found in the vicinity of the dislocation core, as highlighted by yellow arrows in Figure 3g and 3f, which could perform as nuclei and facilitate the growth of ultra-small Pt clusters with random atom arrangements (Figure 3j-l). It indicates an increased chemical reactivity of these defective structures possibly due to their specific coordination manners and the presence of built-in strain.

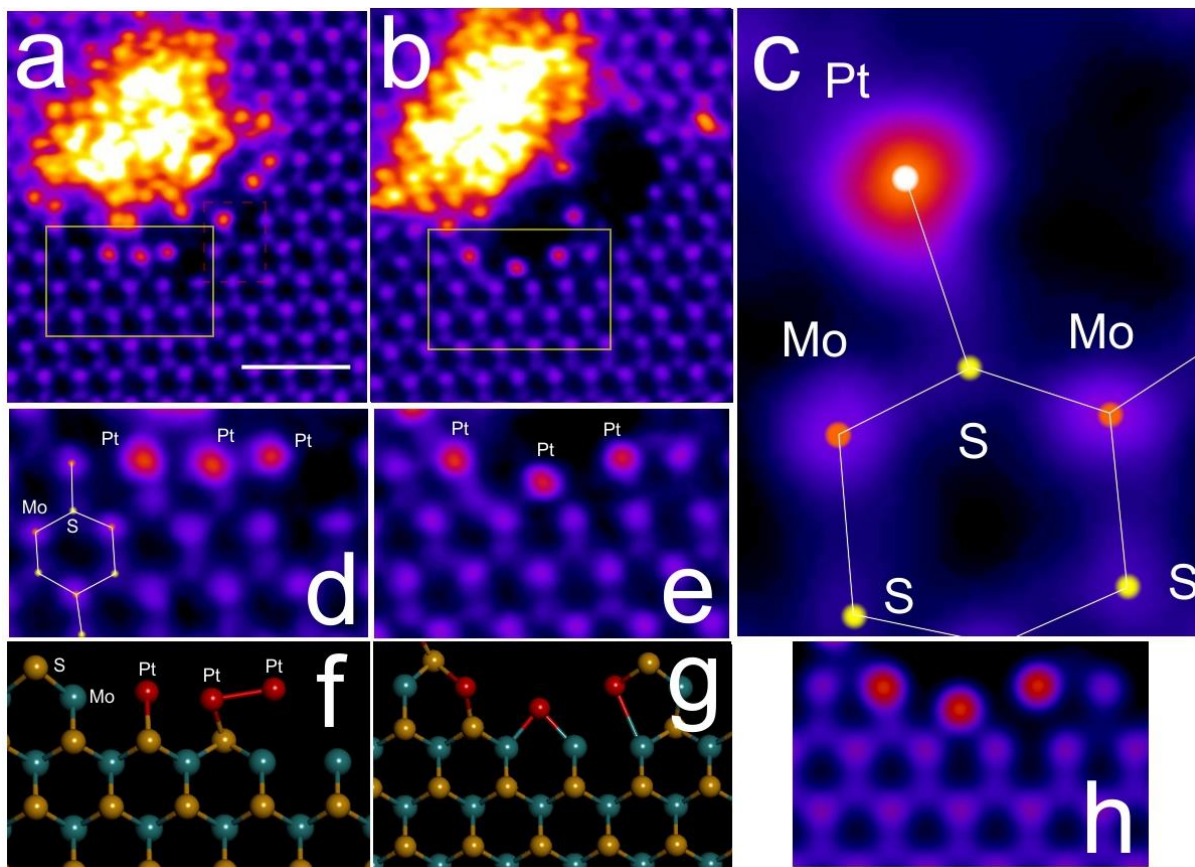


Figure 4. (a) ADF-STEM image of Pt nanocluster within a nanopore at the small-angle GB of MoS₂ monolayer. The scale bar: 1nm. (b) ADF-STEM image taken 30s after (a). (c) Higher magnification of the red boxed region in (a) showing the Pt bonding to S site at the edge. (d) Higher magnification ADF-STEM image from the yellow box in (a), showing single Pt atoms attached to the edge. (e) Higher magnification ADF-STEM image from the yellow box area in (b). (f) Schematic atomic model representation of the ADF-STEM image in (d) with three Pt atoms attached to the MoS₂ edge. (g) Schematic atomic model representation of (e). (h) Multislice ADF-STEM image simulation using the atomic model from (g), showing similar contrast to the experimental image in (e).

To show that some of the Pt nanoclusters are formed within the holes at the GBs, we examined the area in more detail. Figure 4 shows the Pt nanocluster within a small nanopore on the small-angle GB, with some part of the open nanopore visible in the bottom section. Pt atoms with higher contrast in the ADF-STEM image are seen attached to various edge sites around the nanopore, figure 4a. An image taken 30s later shows the reconstruction of the Pt atomic bonding sites due to the electron beam

irradiation causing some structural modifications. Figure 4c shows the high magnification view of the red boxed area in figure 4a, with the Pt atom bonded to the S site. Figures 4d and e show the yellow boxed regions from 4a and b respectively and reveal the various Pt binding sites at the edge. In figure 4d, the two Pt atoms on the left are bonded to S atoms, with the third Pt atom bonded to the middle Pt atom forming Pt-Pt bond. In the next frame, figure 4e, the middle Pt atom is now bonded to the two Mo atoms, with the S atoms previously there being sputtered away by the electron beam. Schematic atomic models are shown below in figures f and g, respectively. A multislice ADF-STEM image simulation, figure 4h, based on the atomic model in figure g, shows a good match for the Pt contrast and positions relative to the MoS₂ lattice. These images show that Pt can bond to both S and Mo sites at the edge by natural decoration during the thermal decomposition rather than by the electron beam induced reconstruction (Figure S5 in SI).

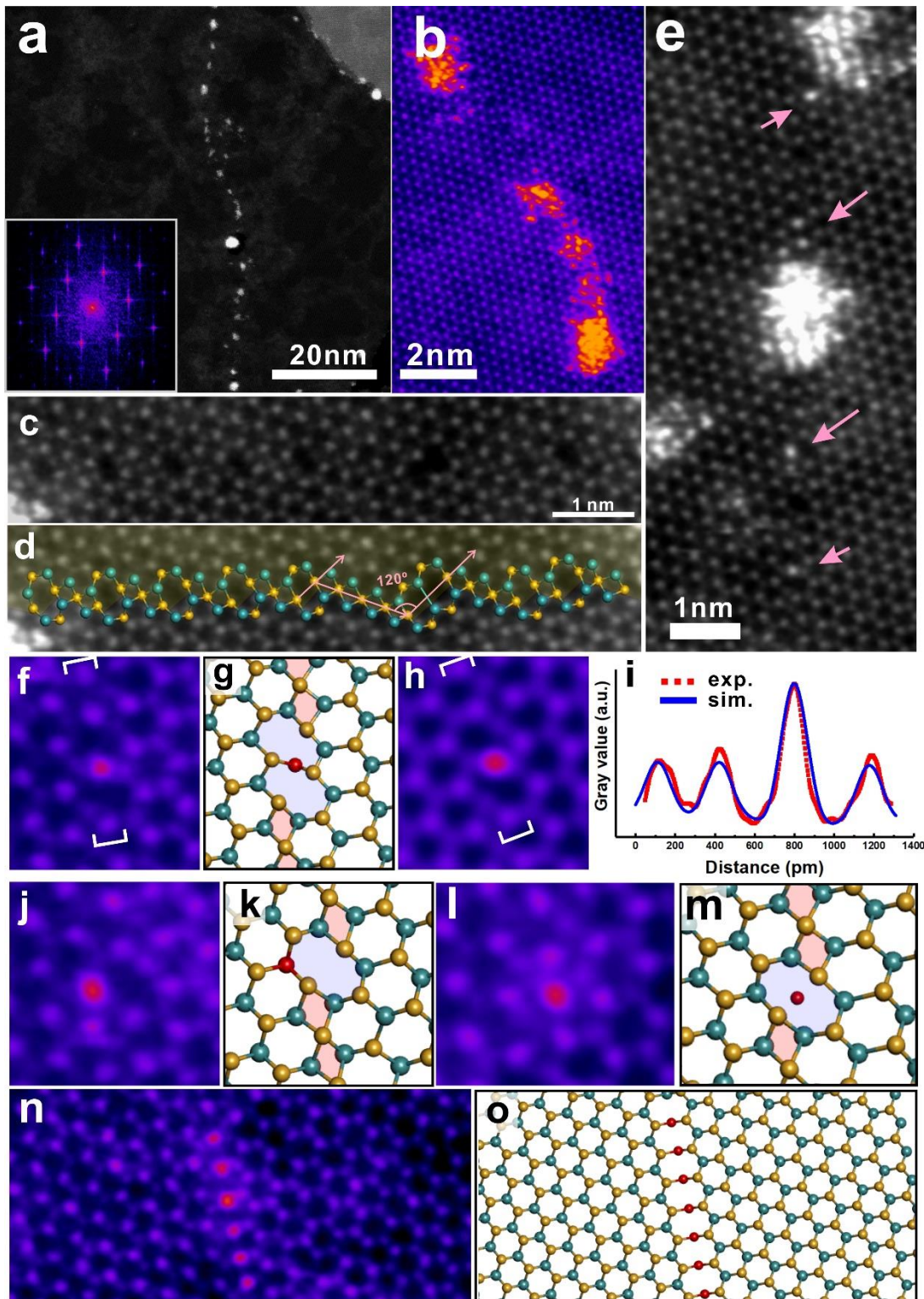


Figure 5. (a) Low-mag ADF-STEM image showing the decoration of Pt nanocrystals on a APB. Inset is the FFT of (a). (b) Medium-mag ADF-STEM image exhibiting the random and non-uniform attachment of Pt nanoparticles along the APB. (c) High-mag ADF-STEM image showing the atomic structure of the APB. (d) Overlay of atomic models of 4- and 8-membered rings in a straight APB with the ADF-STEM image in (c), with a semi-transparent mask in yellow covered in

the upper grain. Green and yellow spheres represent Mo and S atoms, respectively. (e) ADF-STEM image showing the existence of single Pt atoms substitution at the APB, indicated by pink arrows. (f,j,l,n) High-mag ADF-STEM images showing the Pt atom sitting in several typical locations of the APB. (g,k,m,o) Atomic models corresponding to ADF-STEM images in (f), (j), (l), and (n), respectively. The single Pt atom is represented by the red sphere. (h) Multislice ADF-STEM image simulation corresponding to the atomic model in (f). (i) Intensity line profiles measured from the selected area marked by the white square brackets in (f) and (h), respectively.

The Pt decoration of APBs is different from that of small-angle GBs. Pt nanocrystals localize on the APB non-uniformly with a random dispersion rather than situating at discrete dislocation cores on small-angle GBs with an even spacing (Figure 5a,b). This could be ascribed to the continuous but aperiodic 8- and 4-fold rings aligning along the APB with peculiar coordination numbers, as illustrated in Figure 1d. Free combination of 4- and 8-fold rings lead to the structural diversity of APB. It can extend straightly with occasional kinks. Figure 5c is a high-mag ADF-STEM image of a linearly-extended APB with corresponding atomic models overlaid in Figure 5d. Discrete 8-fold rings are commonly connected by short strings of 4-fold rings in arbitrary lengths, which are constructed by point sharing at 2S sites and extend along one zigzag lattice direction. Octagons and tetragons atomically stitch with edge sharing. Sometimes 8-fold rings can directly link together in parallel with edge sharing but could lead to the loss of double S atoms on the joint side. The orientation of the 8-fold ring is along another zigzag lattice orientation of MoS₂, which has a tilt angle of integral multiples of 60° with respect to that of the string of 4-fold rings, as depicted by pink arrow in Figure 5d. Therefore, different combinations of 8- and 4-fold rings realize the flexibility of the APB direction in the macroscopic scale.

Figure 5e is a general view showing several single Pt atoms residing along an APB free of contaminations, as marked by pink arrows. Figure 5f,j,l,n list some typical examples of single Pt atom

substitution at defective sites in magnified images with corresponding atomic models shown in Figure 5g,k,m,o. Surprisingly, distinct from the case of single Pt atom interaction with the pristine MoS₂, where Pt atoms prefer to localize at S vacancy sites,²⁹ Pt atoms at APB are prone to substituting for Mo atoms at 8-fold rings of APB (Figure 5f,g). Figure 5h is the multislice ADF-STEM image simulation based on the atomic model in figure 5f, which matches with the experimental image of figure 5f well. Intensity line profiles (Figure 5i) show a good contrast match between the experimental image (Figure 5f) and the simulation of a substitutional Pt atom in the place of Mo (Figure 5h), which excludes the possibility of single Pt atom sitting on top of the Mo site. A row of Mo atoms in octagons can be replaced by Pt atoms simultaneously (Figure 5n,o). In addition, single Pt atom can also reside on the hollow center of an 8-fold ring owing to the sufficient space of an octagon and the diverse coordination manner of Pt with d orbitals.

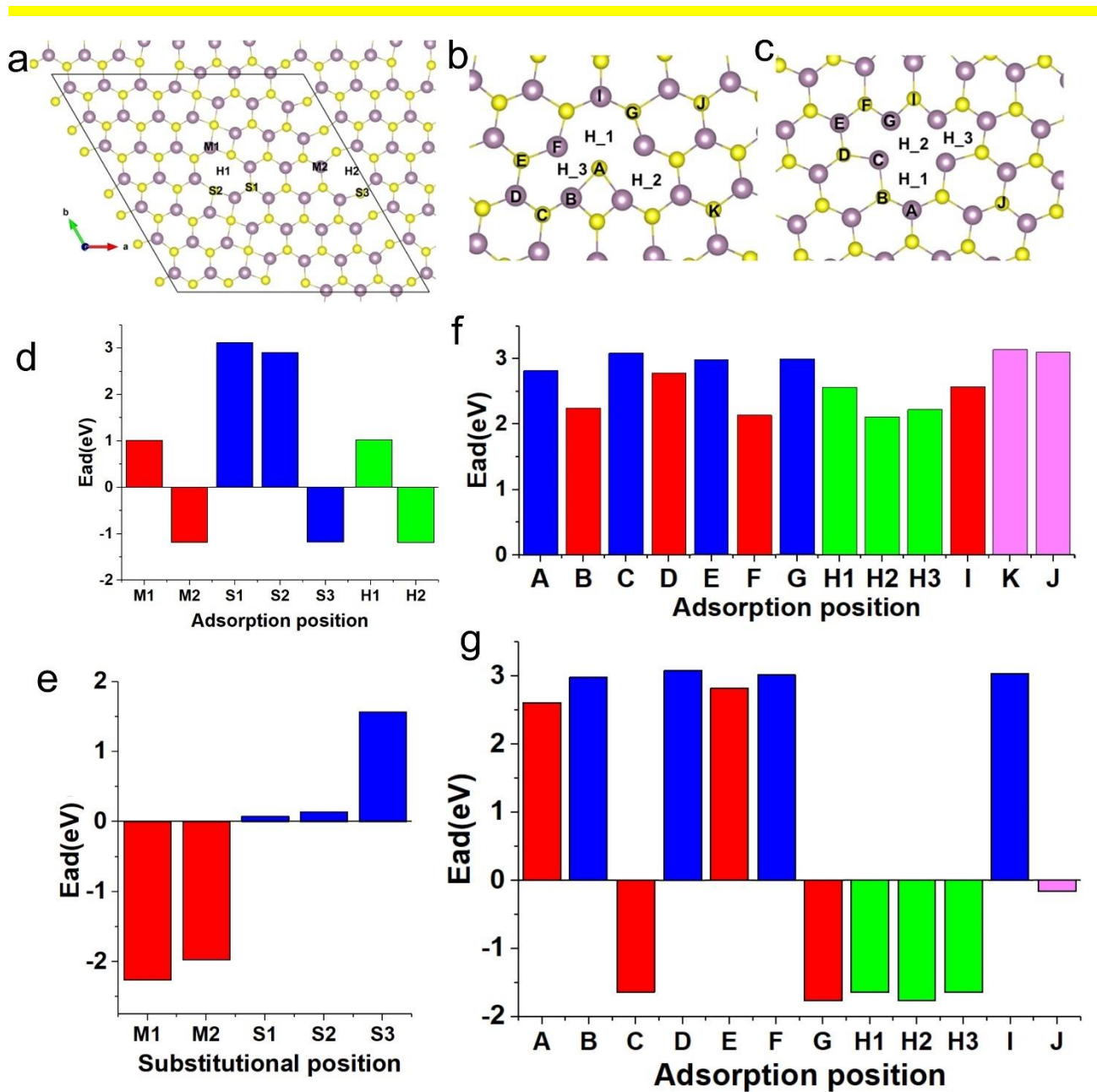


Figure 6. (a) DFT-relaxed atomic model involving typical defective structures in APBs on monolayer MoS₂ with denotations showing atomic sites studied in the DFT calculations for the adsorption or substitution of the single Pt atom. (b,c) DFT-relaxed 6|4 and 5|8|5 dislocation core configurations in the small-angle GB, respectively, with denotations showing atomic sites studied in DFT calculations for the adsorption of the single Pt atom. (d) Bar chart showing the adsorption energy of the single Pt atom on top of the atoms in APBs denoted in (a). Red, blue and green columns represent Mo, S and hollow sites on the APB for Pt adsorption, respectively. (e) Bar chart showing the adsorption energy of the single Pt atom when it substitutes the atoms in APBs denoted in (a). (f, g) Bar charts showing the adsorption energy of the single Pt atom on top of the atoms of dislocation cores in small-angle GBs denoted in (b) and (c), respectively. Red, blue and

green columns represent Mo, S and hollow sites on the small-angle GB for Pt adsorption, respectively, while the pink column represents S sites beside the small-angle GB.

To get the insight of the Pt interactions with the MoS₂ grain boundary, theoretical calculations based on Density Functional Theory (DFT) were carried out to study on the adsorption energy through the MoS₂ grain boundaries, detailed settings listed in the Experimental Section. It is a challenge to model the grain boundary in a periodic model. Here we proposed two different solutions for the small angle and APB grain boundaries, respectively. For the small angle grain boundaries (6|4 and 5|8|5), the dislocation cores were treated as the central of the large cell with the atoms outside the core area kept fixed. The interaction between the Pt atom with the atoms outside the core area is in the same range (~3 eV) with the pristine MoS₂ (Figure 6f,g). For the APB, a supercell with lattice parameters of 7*7 pristine MoS₂ supercell was adopted which co-exists 4|4|8 (Figure 5g, k and m) and 8|8|8 dislocations (Figure 5o), shown in Figure S6 with all the coordinates listed in section S8 of SI. To validate the accuracy of this model, Bader charge analysis⁴⁴ was carried out. Our results show that the charge of the Mo in the shadow area (Figure S6) is 4.99 against 5.00 in the pristine one. While, those Mo in the 8-member rings is 4.95. It implies that further electron transfer from Mo to S induced by the dislocations. Hence, our proposed models could overcome the obstacle to represent grain boundary at the DFT level.

Atoms in the dislocation positions, denoted in Figure 6a-c were selected to study the Pt adsorption behavior in the dislocation area and around dislocation cores. The adsorption energy was calculated based on the following equation:

$$E_{ad} = E_{total} - E_{MoS_2sub} - E_{Pt}$$

Where the E_{total} is the total energy of the system. E_{MoS_2sub} and E_{Pt} are the energy of the MoS₂ substrate

and the chemical energy of the Pt, which derived from the energy of the bulk Pt. As the results shown in Figure 6d,f and g, Pt atom is exothermic stable at the hollow position of the $8|8|8$ (APB) and $5|8|5$ (small-angle GB) dislocations. Compared with Pt on the pristine MoS₂ in our previous study,²⁹ the dislocations in both APBs and small-angle GBs play as the Pt trapping sites. Unlike the mono-vacancy in pristine MoS₂, where Pt tends to substitute S instead of Mo, it is more energetically favorable to substitute Mo in the APB of MoS₂, as shown in Figure 6e. This phenomenon has also been observed in our experiments, Figure 5 (detailed adsorption values shown in section S7 in SI).

In summary, we have shown the selective nucleation of Pt nanocrystals at GBs on polycrystalline monolayer MoS₂ membranes, serving as indicators to facilitate the visualization of GBs with nanometer-scale width and to track their long-range morphology change during the ADF-STEM imaging. Pt nanoparticles decorated on the small-angle GBs show a homogeneous inter-particle distance as they nucleate on the dislocation cores of GBs, whose spacing is quantitatively related to the GB angle based on the Frank-Bilby equation. It provides an approach to evaluate the GB angle by the measurement of the average Pt inter-particles distance, which, sometimes, is more accessible. Pt nanoclusters on APBs are randomly spaced due to the continuous and linearly-aligned octagonal and tetragonal rings with a random combination on APBs, where both two types of defective configurations can work as trapping sites for Pt. Small holes can be formed at GBs with Pt filling into them and attaching at various edge sites. Single Pt atoms have been observed as substitutional dopants in the place of Mo or adatoms residing at the hollow center of 8-fold rings in APBs. DFT calculations have also been conducted to prove the energetic preference of attracting Pt to dislocations of GBs and to compare the reactivity of different atomic sites with Pt in both the APB and the small-angle GB. These

results give insights into the interaction between different types of GBs of monolayer MoS₂ with Pt dopants in various sizes, ranging from single atom, a few atom clusters to nanocrystals, and may help understand the influence of Pt dopants on monolayer MoS₂ more comprehensively.

Experimental Methods

Synthesis and transfer of monolayer MoS₂

MoS₂ monolayers were grown by a hydrogen-free CVD method under atmospheric pressure with molybdenum trioxide (MoO₃, ≥99.5%, Sigma-Aldrich) and sulphur (S, ≥99.5%, Sigma-Aldrich) powder used as precursors, as previously reported.⁴⁰ SiO₂/Si (300 nm thick SiO₂) chips were used as substrates. To avoid the quench of MoO₃ powder by S vapor during the reaction, an inner tube with MoO₃ powder placed inside was inserted into the outer 1-inch quartz tube, where S powder was positioned. Two furnaces were used to give independent temperature control on both two precursors and the substrate. The typical heating temperatures for S, MoO₃ and SiO₂/Si substrate were ~180, ~300, and ~800 °C, respectively. After the growth, monolayer MoS₂ was transferred to a Si₃N₄ TEM grid (Agar Scientific AG21580). A thin film of poly (methyl methacrylate) (PMMA) was first spin-coated on the MoS₂/SiO₂/Si substrate surface. Subsequently, float the sample on a 1 mol/L potassium hydroxide (KOH) solution to etch SiO₂ away. As soon as the PMMA/MoS₂ film detached from the Si substrate, the film was transferred to the deionized water for several times to remove residuals left by the etchant thoroughly. After that, the PMMA/MoS₂ film was scooped up by a holey Si₃N₄ TEM grid, allowed to dry in the air naturally and baked at 180 °C for 15 minutes. The PMMA scaffold was finally removed by submerging the TEM grid in acetone for 8 hours.

Sample preparation of Pt-doped monolayer MoS₂

A drop of hexachloroplatinic acid (H₂PtCl₆)-ethanol solution (0.025mol/L) was deposited on monolayer MoS₂ transferred on the Si₃N₄ TEM grid and dried in the air. The sample was subsequently positioned in the quartz tube and heated to 350°C for 15 min with the carrier gas of argon, thus converting H₂PtCl₆ to Pt. Finally, the sample was rapidly cooled down by removing it from the hot zone furnace.

Scanning transmission electron microscopy and image processing

ADF-STEM imaging was conducted at room temperature on an aberration-corrected JEOL ARM300CF STEM equipped with a JEOL ETA corrector⁴⁵ operated under an accelerating voltage of 60 kV located in the electron Physical Sciences Imaging Centre (ePSIC) at Diamond Light Source. Dwell times of 5–20 μs and a pixel size of 0.006 nm px⁻¹ were used for imaging. Conditions were a CL aperture of 30 μm, convergence semi-angle of 31.5 mrad, beam current of 44 pA, and inner acquisition angle of 49.5–198 mrad.

Images were processed using the ImageJ software. Two types of false colour LUTs, fire and orange hot, were applied to grayscale images for the enhancement of the visual effect of Pt atom dopants and dislocation cores. A Gaussian blur filter (~2-4 pixels) were used on high-mag ADF-STEM images for smoothing. Atomic models were constructed using the software of Accelrys Discovery Studio Visualizer.

Density functional theory (DFT) calculation

All the calculations carried out based on Density Functional Theory, implanted in Vienna ab-initio Package (VASP).^{46,47} The plane wave augment (PAW) potential is adopted to treat the core electron,

with the wave function cut off of 500 eV.⁴⁸ The exchange-correlation interaction was treated by the generalized gradient approximation (GGA) using Perdew-Burke-Ernzerhof exchange-correlation functional.⁴⁹ The energy and forces converged to 10⁻⁵ eV and 0.01 eV/Å, respectively. The K-points were sampled by gamma-only. The dipole correction was considered during the calculations.

The two representative models for small-angle grain boundary of MoS₂ (Figure S7), which depicted from our experimental observation in Figure 3e, f, g and h, were set in a 50*50*20 box. The model 1 and 2 consist of 202 and 204 atoms, respectively. To study the Pt interaction with the defect central, the atoms inside of the highlighted red dash line were fully relaxed, while all other atoms were kept fixed during the whole calculations.

Acknowledgements

JHW thanks the support from the Royal Society and the ERC (grant no: 725258 CoG 2016 LATO).

SW thanks the China Scholarship Council for support.

References

- (1) Radisavljevic, B.; Radenovic, A.; Brivio, J.; Giacometti, V.; Kis, A. Single-Layer MoS₂ Transistors. *Nat. Nanotechnol.* **2011**, *6*, 147–150.
- (2) Wang, Q. H.; Kalantar-Zadeh, K.; Kis, A.; Coleman, J. N.; Strano, M. S. Electronics and Optoelectronics of Two-Dimensional Transition Metal Dichalcogenides. *Nat. Nanotechnol.* **2012**, *7*, 699–712.
- (3) Ganatra, R.; Zhang, Q. Few Layer MoS₂: A Promising Layered Semiconductor. *ACS Nano* **2014**, *8*, 4074–4099.
- (4) Amani, M.; Chin, M. L.; Birdwell, a. G.; O'Regan, T. P.; Najmaei, S.; Liu, Z.; Ajayan, P.

M.; Lou, J.; Dubey, M. Electrical Performance of Monolayer MoS₂ Field-Effect Transistors Prepared by Chemical Vapor Deposition. *Appl. Phys. Lett.* **2013**, *102*, 193107.

- (5) Liu, G.; Robertson, A. W.; Li, M. M.-J.; Kuo, W. C. H.; Darby, M. T.; Muhieddine, M. H.; Lin, Y.-C.; Suenaga, K.; Stamatakis, M.; Warner, J. H.; *et al.* MoS₂ Monolayer Catalyst Doped with Isolated Co Atoms for the Hydrodeoxygenation Reaction. *Nat. Chem.* **2017**, *9*, 810–816.
- (6) Deng, J.; Li, H.; Xiao, J.; Tu, Y.; Deng, D.; Yang, H.; Tian, H.; Li, J.; Ren, P.; Bao, X. Triggering the Electrocatalytic Hydrogen Evolution Activity of Inert Two-Dimensional MoS₂ Surface via Single-Atom Metal Doping. *Energy Environ. Sci.* **2015**, *8*, 1594–1601.
- (7) Dai, X.; Du, K.; Li, Z.; Liu, M.; Ma, Y.; Sun, H.; Zhang, X.; Yang, Y. Co-Doped MoS₂ Nanosheets with the Dominant CoMoS Phase Coated on Carbon as an Excellent Electrocatalyst for Hydrogen Evolution. *ACS Appl. Mater. Interfaces* **2015**, *7*, 27242–27253.
- (8) Li, S.; Wang, S.; Salamone, M. M.; Robertson, A. W.; Nayak, S.; Kim, H.; Tsang, S. E.; Pasta, M.; Warner, J. H. Edge-Enriched 2D MoS₂ Thin Films Grown by Chemical Vapor Deposition for Enhanced Catalytic Performance. *ACS Catal.* **2017**, *7*, 877–886.
- (9) Kang, K.; Xie, S.; Huang, L.; Han, Y.; Huang, P. Y.; Mak, K. F.; Kim, C.-J.; Muller, D.; Park, J. High-Mobility Three-Atom-Thick Semiconducting Films with Wafer-Scale Homogeneity. *Nature* **2015**, *520*, 656–660.
- (10) Wang, S.; Pacios, M.; Bhaskaran, H.; Warner, J. H. Substrate Control for Large Area Continuous Films of Monolayer MoS₂ by Atmospheric Pressure Chemical Vapor Deposition. *Nanotechnology* **2016**, *27*, 85604–85611.

- (11) Senthilkumar, V.; Tam, L.; Kim, Y.; Sim, Y. Direct Vapor Phase Growth Process and Robust Photoluminescence Properties of Large Area MoS₂ Layer. *Nano Res.* **2014**, *7*, 1759–1768.
- (12) Lee, Y.-H.; Zhang, X.-Q.; Zhang, W.; Chang, M.-T.; Lin, C.-T.; Chang, K.-D.; Yu, Y.-C.; Wang, J. T.-W.; Chang, C.-S.; Li, L.-J.; *et al.* Synthesis of Large-Area MoS₂ Atomic Layers with Chemical Vapor Deposition. *Adv. Mater.* **2012**, *24*, 2320–2325.
- (13) Marzari, N.; Sanchez, O. L.; Kung, Y.; Krasnozhan, D.; Chen, M.; Bertolazzi, S.; Gillet, P.; Fontcuberta, A.; Radenovic, A.; Kis, A. Large-Area Epitaxial Monolayer MoS₂. *ACS Nano* **2015**, *9*, 4611–4620.
- (14) Liu, K.-K.; Zhang, W.; Lee, Y.-H.; Lin, Y.-C.; Chang, M.-T.; Su, C.-Y.; Chang, C.-S.; Li, H.; Shi, Y.; Zhang, H.; *et al.* Growth of Large-Area and Highly Crystalline MoS₂ Thin Layers on Insulating Substrates. *Nano Lett.* **2012**, *12*, 1538–1544.
- (15) Zhou, W.; Zou, X.; Najmaei, S.; Liu, Z.; Shi, Y.; Kong, J.; Lou, J.; Ajayan, P. M.; Yakobson, B. I.; Idrobo, J.-C. Intrinsic Structural Defects in Monolayer Molybdenum Disulfide. *Nano Lett.* **2013**, *13*, 2615–2622.
- (16) van der Zande, A. M.; Huang, P. Y.; Chenet, D. A.; Berkelbach, T. C.; You, Y.; Lee, G.-H.; Heinz, T. F.; Reichman, D. R.; Muller, D. A.; Hone, J. C. Grains and Grain Boundaries in Highly Crystalline Monolayer Molybdenum Disulfide. *Nat. Mater.* **2013**, *12*, 554–561.
- (17) Kim, D. W.; Kim, Y. H.; Jeong, H. S.; Jung, H.-T. Direct Visualization of Large-Area Graphene Domains and Boundaries by Optical Birefringency. *Nat. Nanotechnol.* **2011**, *7*, 29–34.
- (18) Kim, D. W.; Ok, J. M.; Jung, W. Bin; Kim, J. S.; Kim, S. J.; Choi, H. O.; Kim, Y. H.; Jung, H.

T. Direct Observation of Molybdenum Disulfide, MoS₂, Domains by Using a Liquid

Crystalline Texture Method. *Nano Lett.* **2015**, *15*, 229–234.

- (19) Duong, D. L.; Han, G. H.; Lee, S. M.; Gunes, F.; Kim, E. S.; Kim, S. T.; Kim, H.; Ta, Q. H.; So, K. P.; Yoon, S. J.; *et al.* Probing Graphene Grain Boundaries with Optical Microscopy. *Nature* **2012**, *490*, 235–239.
- (20) Karvonen, L.; Säynätjoki, A.; Huttunen, M. J.; Autere, A.; Amirsolaimani, B.; Li, S.; Norwood, R. A.; Peyghambarian, N.; Lipsanen, H.; Eda, G.; *et al.* Rapid Visualization of Grain Boundaries in Monolayer MoS₂ by Multiphoton Microscopy. *Nat. Commun.* **2017**, *8*, 15714.
- (21) Najmaei, S.; Liu, Z.; Zhou, W.; Zou, X.; Shi, G.; Lei, S.; Yakobson, B. I.; Idrobo, J.-C.; Ajayan, P. M.; Lou, J. Vapour Phase Growth and Grain Boundary Structure of Molybdenum Disulphide Atomic Layers. *Nat. Mater.* **2013**, *12*, 754–759.
- (22) Krivanek, O. L.; Chisholm, M. F.; Nicolosi, V.; Pennycook, T. J.; Corbin, G. J.; Dellby, N.; Murfitt, M. F.; Own, C. S.; Szilagy, Z. S.; Oxley, M. P.; *et al.* Atom-by-Atom Structural and Chemical Analysis by Annular Dark-Field Electron Microscopy. *Nature* **2010**, *464*, 571–574.
- (23) Lin, Y.-C.; Dumcenco, D. O.; Huang, Y.-S.; Suenaga, K. Atomic Mechanism of the Semiconducting-to-Metallic Phase Transition in Single-Layered MoS₂. *Nat. Nanotechnol.* **2014**, *9*, 391–396.
- (24) Yan, A.; Chen, W.; Ophus, C.; Ciston, J.; Lin, Y.; Persson, K.; Zettl, A. Identifying Different Stacking Sequences in Few-Layer CVD-Grown MoS₂ by Low-Energy Atomic-Resolution Scanning Transmission Electron Microscopy. *Phys. Rev. B* **2016**, *93*, 041420.

- (25) Chen, Q.; Li, H.; Xu, W.; Wang, S.; Sawada, H.; Allen, C. S.; Kirkland, A. I.; Grossman, J. C.; Warner, J. H. Atomically Flat Zigzag Edges in Monolayer MoS₂ by Thermal Annealing. *Nano Lett.* **2017**, *17*, 5502–5507.
- (26) Wang, S.; Sawada, H.; Chen, Q.; Han, G. G. D.; Allen, C.; Kirkland, A. I.; Warner, J. H. In Situ Atomic-Scale Studies of the Formation of Epitaxial Pt Nanocrystals on Monolayer Molybdenum Disulfide. *ACS Nano* **2017**, *11*, 9057–9067.
- (27) Wang, S.; Li, H.; Sawada, H.; Allen, C. S.; Kirkland, A. I.; Grossman, J. C.; Warner, J. H. Atomic Structure and Formation Mechanism of Sub-Nanometer Pores in 2D Monolayer MoS₂. *Nanoscale* **2017**, *9*, 6417–6426.
- (28) Lin, Y. C.; Dumcenco, D. O.; Komsa, H.-P.; Niimi, Y.; Krasheninnikov, A. V.; Huang, Y.-S.; Suenaga, K. Properties of Individual Dopant Atoms in Single-Layer MoS₂: Atomic Structure, Migration, and Enhanced Reactivity. *Adv. Mater.* **2014**, *26*, 2857–2861.
- (29) Li, H.; Wang, S.; Samuels, T.; Han, G. G. D.; Allen, C. S.; Kirkland, A. I.; Grossman, J. C.; Jamie, H. Atomic Structure and Dynamics of Single Pt Atom Interactions with Monolayer MoS₂. *ACS Nano* **2017**, *11*, 3392–3403.
- (30) Robertson, A. W.; Lin, Y.; Wang, S.; Sawada, H.; Allen, C. S.; Chen, Q.; Lee, S.; Lee, G.; Han, S.; Yoon, E.; *et al.* Atomic Structure and Spectroscopy of Single Metal (Cr, V) Substitutional Dopants in Monolayer MoS₂. *ACS Nano* **2016**, *10*, 10227–10236.
- (31) Kim, K.; Lee, H.-B.-R.; Johnson, R. W.; Tanskanen, J. T.; Liu, N.; Kim, M.-G.; Pang, C.; Ahn, C.; Bent, S. F.; Bao, Z. Selective Metal Deposition at Graphene Line Defects by Atomic Layer Deposition. *Nat. Commun.* **2014**, *5*, 4781.

- (32) Frank, F. . Martensite. *Acta Metall.* **1953**, *1*, 15–21.
- (33) Bullough, R.; Bilby, B. A. Continuous Distributions of Dislocations: Surface Dislocations and the Crystallography of Martensitic Transformations. *Proc. Phys. Soc.* **1956**, *69*, 1276–1286.
- (34) Bilby, B. A.; Bullough, R.; Smith, E. Continuous Distributions of Dislocations: A New Application of the Methods of Non-Riemannian Geometry. *Proc. R. Soc.* **1955**, *231*, 263–273.
- (35) Wang, L.; Teng, J.; Liu, P.; Hirata, A.; Ma, E.; Zhang, Z.; Chen, M.; Han, X. Grain Rotation Mediated by Grain Boundary Dislocations in Nanocrystalline Platinum. *Nat. Commun.* **2014**, *5*, 4402.
- (36) Hirth, J. P.; Pond, R. C.; Hoagland, R. G.; Liu, X. Y.; Wang, J. Interface Defects, Reference Spaces and the Frank-Bilby Equation. *Prog. Mater. Sci.* **2013**, *58*, 749–823.
- (37) Kitching, H.; Shiers, M. J.; Kenyon, A. J.; Parkin, I. P. Self-Assembly of Metallic Nanoparticles into One Dimensional Arrays. *J. Mater. Chem. A* **2013**, *1*, 6985.
- (38) Mookath, J. H.; Henzie, J. One-Dimensional Aluminum Nanoparticle Chains: The Influence of Interparticle Spacing and Chain Length on the Plasmon Coupling Behavior. *J. Mater. Chem. C* **2017**, *5*, 4379–4383.
- (39) Hong, M.; Wu, L.; Tian, L.; Zhu, J. Controlled Assembly of Au, Ag, and Pt Nanoparticles with Chitosan. *Chem. Eur. J.* **2009**, *15*, 5935–5941.
- (40) Wang, S.; Wang, X.; Warner, J. H. All Chemical Vapor Deposition Growth of MoS₂:h-BN Vertical van Der Waals Heterostructures. *ACS Nano* **2015**, *9*, 5246–5254.
- (41) Wang, S.; Qin, Z.; Jung, G. S.; Martin-Martinez, F. J.; Zhang, K.; Buehler, M. J.; Warner, J. H. Atomically Sharp Crack Tips in Monolayer MoS₂ and Their Enhanced Toughness by

Vacancy Defects. *ACS Nano* **2016**, *10*, 9831–9839.

- (42) Wang, S.; Lee, G.-D.; Lee, S.; Yoon, E.; Warner, J. H. Detailed Atomic Reconstruction of Extended Line Defects in Monolayer MoS₂. *ACS Nano* **2016**, *10*, 5419–5430.
- (43) Elibol, K.; Susi, T.; O'Brien, M.; Bayer, B.; Pennycook, T. J.; McEvoy, N.; Duesberg, G.; Meyer, Y. C.; Kotakoski, J. Grain Boundary-Mediated Nanopores in Molybdenum Disulfide Grown by Chemical Vapor Deposition. *Nanoscale* **2017**, *9*, 1591.
- (1) Radisavljevic, B.; Radenovic, A.; Brivio, J.; Giacometti, V.; Kis, A. Single-Layer MoS₂ Transistors. *Nat. Nanotechnol.* **2011**, *6*, 147–150.
- (2) Wang, Q. H.; Kalantar-Zadeh, K.; Kis, A.; Coleman, J. N.; Strano, M. S. Electronics and Optoelectronics of Two-Dimensional Transition Metal Dichalcogenides. *Nat. Nanotechnol.* **2012**, *7*, 699–712.
- (3) Ganatra, R.; Zhang, Q. Few Layer MoS₂: A Promising Layered Semiconductor. *ACS Nano* **2014**, *8*, 4074–4099.
- (4) Amani, M.; Chin, M. L.; Birdwell, a. G.; O'Regan, T. P.; Najmaei, S.; Liu, Z.; Ajayan, P. M.; Lou, J.; Dubey, M. Electrical Performance of Monolayer MoS₂ Field-Effect Transistors Prepared by Chemical Vapor Deposition. *Appl. Phys. Lett.* **2013**, *102*, 193107.
- (5) Liu, G.; Robertson, A. W.; Li, M. M.-J.; Kuo, W. C. H.; Darby, M. T.; Muhieddine, M. H.; Lin, Y.-C.; Suenaga, K.; Stamatakis, M.; Warner, J. H.; *et al.* MoS₂ Monolayer Catalyst Doped with Isolated Co Atoms for the Hydrodeoxygenation Reaction. *Nat. Chem.* **2017**, *9*, 810–816.
- (6) Deng, J.; Li, H.; Xiao, J.; Tu, Y.; Deng, D.; Yang, H.; Tian, H.; Li, J.; Ren, P.; Bao, X. Triggering the Electrocatalytic Hydrogen Evolution Activity of Inert Two-Dimensional MoS₂

Surface via Single-Atom Metal Doping. *Energy Environ. Sci.* **2015**, *8*, 1594–1601.

- (7) Dai, X.; Du, K.; Li, Z.; Liu, M.; Ma, Y.; Sun, H.; Zhang, X.; Yang, Y. Co-Doped MoS₂ Nanosheets with the Dominant CoMoS Phase Coated on Carbon as an Excellent Electrocatalyst for Hydrogen Evolution. *ACS Appl. Mater. Interfaces* **2015**, *7*, 27242–27253.
- (8) Li, S.; Wang, S.; Salamone, M. M.; Robertson, A. W.; Nayak, S.; Kim, H.; Tsang, S. E.; Pasta, M.; Warner, J. H. Edge-Enriched 2D MoS₂ Thin Films Grown by Chemical Vapor Deposition for Enhanced Catalytic Performance. *ACS Catal.* **2017**, *7*, 877–886.
- (9) Kang, K.; Xie, S.; Huang, L.; Han, Y.; Huang, P. Y.; Mak, K. F.; Kim, C.-J.; Muller, D.; Park, J. High-Mobility Three-Atom-Thick Semiconducting Films with Wafer-Scale Homogeneity. *Nature* **2015**, *520*, 656–660.
- (10) Wang, S.; Pacios, M.; Bhaskaran, H.; Warner, J. H. Substrate Control for Large Area Continuous Films of Monolayer MoS₂ by Atmospheric Pressure Chemical Vapor Deposition. *Nanotechnology* **2016**, *27*, 85604–85611.
- (11) Senthilkumar, V.; Tam, L.; Kim, Y.; Sim, Y. Direct Vapor Phase Growth Process and Robust Photoluminescence Properties of Large Area MoS₂ Layer. *Nano Res.* **2014**, *7*, 1759–1768.
- (12) Lee, Y.-H.; Zhang, X.-Q.; Zhang, W.; Chang, M.-T.; Lin, C.-T.; Chang, K.-D.; Yu, Y.-C.; Wang, J. T.-W.; Chang, C.-S.; Li, L.-J.; *et al.* Synthesis of Large-Area MoS₂ Atomic Layers with Chemical Vapor Deposition. *Adv. Mater.* **2012**, *24*, 2320–2325.
- (13) Marzari, N.; Sanchez, O. L.; Kung, Y.; Krasnozhan, D.; Chen, M.; Bertolazzi, S.; Gillet, P.; Fontcuberta, A.; Radenovic, A.; Kis, A. Large-Area Epitaxial Monolayer MoS₂. *ACS Nano* **2015**, *9*, 4611–4620.

- (14) Liu, K.-K.; Zhang, W.; Lee, Y.-H.; Lin, Y.-C.; Chang, M.-T.; Su, C.-Y.; Chang, C.-S.; Li, H.; Shi, Y.; Zhang, H.; *et al.* Growth of Large-Area and Highly Crystalline MoS₂ Thin Layers on Insulating Substrates. *Nano Lett.* **2012**, *12*, 1538–1544.
- (15) Zhou, W.; Zou, X.; Najmaei, S.; Liu, Z.; Shi, Y.; Kong, J.; Lou, J.; Ajayan, P. M.; Yakobson, B. I.; Idrobo, J.-C. Intrinsic Structural Defects in Monolayer Molybdenum Disulfide. *Nano Lett.* **2013**, *13*, 2615–2622.
- (16) van der Zande, A. M.; Huang, P. Y.; Chenet, D. A.; Berkelbach, T. C.; You, Y.; Lee, G.-H.; Heinz, T. F.; Reichman, D. R.; Muller, D. A.; Hone, J. C. Grains and Grain Boundaries in Highly Crystalline Monolayer Molybdenum Disulfide. *Nat. Mater.* **2013**, *12*, 554–561.
- (17) Kim, D. W.; Kim, Y. H.; Jeong, H. S.; Jung, H.-T. Direct Visualization of Large-Area Graphene Domains and Boundaries by Optical Birefringency. *Nat. Nanotechnol.* **2011**, *7*, 29–34.
- (18) Kim, D. W.; Ok, J. M.; Jung, W. Bin; Kim, J. S.; Kim, S. J.; Choi, H. O.; Kim, Y. H.; Jung, H. T. Direct Observation of Molybdenum Disulfide, MoS₂, Domains by Using a Liquid Crystalline Texture Method. *Nano Lett.* **2015**, *15*, 229–234.
- (19) Duong, D. L.; Han, G. H.; Lee, S. M.; Gunes, F.; Kim, E. S.; Kim, S. T.; Kim, H.; Ta, Q. H.; So, K. P.; Yoon, S. J.; *et al.* Probing Graphene Grain Boundaries with Optical Microscopy. *Nature* **2012**, *490*, 235–239.
- (20) Karvonen, L.; Säynätjoki, A.; Huttunen, M. J.; Autere, A.; Amirsolaimani, B.; Li, S.; Norwood, R. A.; Peyghambarian, N.; Lipsanen, H.; Eda, G.; *et al.* Rapid Visualization of Grain Boundaries in Monolayer MoS₂ by Multiphoton Microscopy. *Nat. Commun.* **2017**, *8*,

15714.

- (21) Najmaei, S.; Liu, Z.; Zhou, W.; Zou, X.; Shi, G.; Lei, S.; Yakobson, B. I.; Idrobo, J.-C.; Ajayan, P. M.; Lou, J. Vapour Phase Growth and Grain Boundary Structure of Molybdenum Disulphide Atomic Layers. *Nat. Mater.* **2013**, *12*, 754–759.
- (22) Krivanek, O. L.; Chisholm, M. F.; Nicolosi, V.; Pennycook, T. J.; Corbin, G. J.; Dellby, N.; Murfitt, M. F.; Own, C. S.; Szilagy, Z. S.; Oxley, M. P.; *et al.* Atom-by-Atom Structural and Chemical Analysis by Annular Dark-Field Electron Microscopy. *Nature* **2010**, *464*, 571–574.
- (23) Lin, Y.-C.; Dumcenco, D. O.; Huang, Y.-S.; Suenaga, K. Atomic Mechanism of the Semiconducting-to-Metallic Phase Transition in Single-Layered MoS₂. *Nat. Nanotechnol.* **2014**, *9*, 391–396.
- (24) Yan, A.; Chen, W.; Ophus, C.; Ciston, J.; Lin, Y.; Persson, K.; Zettl, A. Identifying Different Stacking Sequences in Few-Layer CVD-Grown MoS₂ by Low-Energy Atomic-Resolution Scanning Transmission Electron Microscopy. *Phys. Rev. B* **2016**, *93*, 41420.
- (25) Chen, Q.; Li, H.; Xu, W.; Wang, S.; Sawada, H.; Allen, C. S.; Kirkland, A. I.; Grossman, J. C.; Warner, J. H. Atomically Flat Zigzag Edges in Monolayer MoS₂ by Thermal Annealing. *Nano Lett.* **2017**, *17*, 5502–5507.
- (26) Wang, S.; Sawada, H.; Chen, Q.; Han, G. G. D.; Allen, C.; Kirkland, A. I.; Warner, J. H. In Situ Atomic-Scale Studies of the Formation of Epitaxial Pt Nanocrystals on Monolayer Molybdenum Disulfide. *ACS Nano* **2017**, *11*, 9057–9067.
- (27) Wang, S.; Li, H.; Sawada, H.; Allen, C. S.; Kirkland, A. I.; Grossman, J. C.; Warner, J. H. Atomic Structure and Formation Mechanism of Sub-Nanometer Pores in 2D Monolayer MoS

2. *Nanoscale* **2017**, *9*, 6417–6426.

- (28) Lin, Y. C.; Dumcenco, D. O.; Komsa, H.-P.; Niimi, Y.; Krasheninnikov, A. V.; Huang, Y.-S.; Suenaga, K. Properties of Individual Dopant Atoms in Single-Layer MoS₂: Atomic Structure, Migration, and Enhanced Reactivity. *Adv. Mater.* **2014**, *26*, 2857–2861.
- (29) Li, H.; Wang, S.; Samuels, T.; Ggoch, G.; Han, D.; Allen, C. S.; Kirkland, A. I.; Grossman, J. C.; Jamie, H. Atomic Structure and Dynamics of Single Pt Atom Interactions with Monolayer MoS₂. *ACS Nano* **2017**, *11*, 3392–3403.
- (30) Robertson, A. W.; Lin, Y.; Wang, S.; Sawada, H.; Allen, C. S.; Chen, Q.; Lee, S.; Lee, G.; Han, S.; Yoon, E.; *et al.* Atomic Structure and Spectroscopy of Single Metal (Cr, V) Substitutional Dopants in Monolayer MoS₂. *ACS Nano* **2016**, *10*, 10227–10236.
- (31) Kim, K.; Lee, H.-B.-R.; Johnson, R. W.; Tanskanen, J. T.; Liu, N.; Kim, M.-G.; Pang, C.; Ahn, C.; Bent, S. F.; Bao, Z. Selective Metal Deposition at Graphene Line Defects by Atomic Layer Deposition. *Nat. Commun.* **2014**, *5*, 4781.
- (32) Frank, F. . Martensite. *Acta Metall.* **1953**, *1*, 15–21.
- (33) Bullough, R.; Bilby, B. A. Continuous Distributions of Dislocations: Surface Dislocations and the Crystallography of Martensitic Transformations. *Proc. Phys. Soc. Sect. B* **1956**, *69*, 1276–1286.
- (34) Bilby, B. A.; Bullough, R.; Smith, E. Continuous Distributions of Dislocations: A New Application of the Methods of Non-Riemannian Geometry. *Proc. R. Soc. A Math. Phys. Eng. Sci.* **1955**, *231*, 263–273.
- (35) Wang, L.; Teng, J.; Liu, P.; Hirata, A.; Ma, E.; Zhang, Z.; Chen, M.; Han, X. Grain Rotation

Mediated by Grain Boundary Dislocations in Nanocrystalline Platinum. *Nat. Commun.* **2014**, *5*, 4402.

- (36) Hirth, J. P.; Pond, R. C.; Hoagland, R. G.; Liu, X. Y.; Wang, J. Interface Defects, Reference Spaces and the Frank-Bilby Equation. *Prog. Mater. Sci.* **2013**, *58*, 749–823.
- (37) Kitching, H.; Shiers, M. J.; Kenyon, A. J.; Parkin, I. P. Self-Assembly of Metallic Nanoparticles into One Dimensional Arrays. *J. Mater. Chem. A* **2013**, *1*, 6985.
- (38) Makkath, J. H.; HENZIE, J. One-Dimensional Aluminum Nanoparticle Chains: The Influence of Interparticle Spacing and Chain Length on the Plasmon Coupling Behavior. *J. Mater. Chem. C* **2017**, *5*, 4379–4383.
- (39) Hong, M.; Wu, L.; Tian, L.; Zhu, J. Controlled Assembly of Au, Ag, and Pt Nanoparticles with Chitosan. *Chem. - A Eur. J.* **2009**, *15*, 5935–5941.
- (40) Wang, S.; Wang, X.; Warner, J. H. All Chemical Vapor Deposition Growth of MoS₂:h-BN Vertical van Der Waals Heterostructures. *ACS Nano* **2015**, *9*, 5246–5254.
- (41) Wang, S.; Qin, Z.; Jung, G. S.; Martin-Martinez, F. J.; Zhang, K.; Buehler, M. J.; Warner, J. H. Atomically Sharp Crack Tips in Monolayer MoS₂ and Their Enhanced Toughness by Vacancy Defects. *ACS Nano* **2016**, *10*, 9831–9839.
- (42) Wang, S.; Lee, G.-D.; Lee, S.; Yoon, E.; Warner, J. H. Detailed Atomic Reconstruction of Extended Line Defects in Monolayer MoS₂. *ACS Nano* **2016**, *10*, 5419–5430.
- (43) Elibol, K.; Susi, T.; O'Brien, M.; Bayer, B.; Pennycook, T. J.; McEvoy, N.; Duesberg, G.; Meyer, Y. C.; Kotakoski, J. Grain Boundary-Mediated Nanopores in Molybdenum Disulfide Grown by Chemical Vapor Deposition. *Nanoscale* **2017**, *9*, 1591.

- (44) Tang, W.; Sanville, E.; Henkelman, G. A Grid-Based Bader Analysis Algorithm without Lattice Bias. *J. Phys. Condens. Matter* **2009**, *21*, 084204.
- (45) Hosokawa, F.; Sawada, H.; Kondo, Y.; Takayanagi, K.; Suenaga, K. Development of Cs and Cc Correctors for Transmission Electron Microscopy. *Microscopy* **2013**, *62*, 23–41.
- (46) Kresse, G.; Furthmüller, J. Efficient Iterative Schemes for Ab Initio Total-Energy Calculations Using a Plane-Wave Basis Set. *Phys. Rev. B* **1996**, *54*, 11169–11186.
- (47) Kresse, G.; Furthmüller, J. Efficiency of Ab-Initio Total Energy Calculations for Metals and Semiconductors Using a Plane-Wave Basis Set. *Comput. Mater. Sci.* **1996**, *6*, 15–50.
- (48) Blochl, P. E. Projector Augmented-Wave Method. *Phys. Rev. B* **1994**, *50*, 17953–17979.
- (49) Perdew, J. P.; Burke, K.; Ernzerhof, M. Generalized Gradient Approximation Made Simple. *Phys. Rev. Lett.* **1996**, *77*, 3865–3868.